Continuum-micromechanical modeling of distributed crazing in rubber-toughened polymers

M. Helbig[a], E. van der Giessen[b], A.H. Clausen[c], Th. Seelig[a1]

[a]Institute of Mechanics, Karlsruhe Institute of Technology, Kaiserstrasse 12, 76131 Karlsruhe, Germany

[b]Zernike Institute for Advanced Materials, University of Groningen, Nijenborgh 4, 9747 AG Groningen, The Netherlands

[c]Structural Impact Laboratory (SIMLab), Department of Structural Engineering, Norwegian University of Science and Technology (NTNU), Rich. Birkelandsvei 1A, NO-7491 Trondheim, Norway

Abstract

A micromechanics based constitutive model is developed that focuses on the effect of distributed crazing in the overall inelastic deformation behavior of rubber-toughened ABS (acrylonitrile-butadiene-styrene) materials. While ABS is known to exhibit crazing *and* shear yielding as inelastic deformation mechanisms, the present work is meant to complement earlier studies where solely shear yielding was considered. In order to analyse the role of either mechanism separately, we here look at the other extreme and assume that the formation and growth of multiple crazes in the glassy matrix between dispersed rubber particles is the major source of overall inelastic strain. This notion is cast into a homogenized material model that explicitly accounts for the specific (cohesive zone-like) kinematics of craze opening as well as for microstructural parameters such as the volume fraction and size of the rubber particles. Numerical simulations on single-edge-notch-tension (SENT) specimens are performed in order to investigate effects of the microstructure on the overall fracture behavior. Experimental results for a commercial ABS material are reported which are partially used to calibrate and to verify the constitutive model, but which also illustrate its limitations.

[1]Corresponding author: Tel.:+49-721-608-43714; Fax.:+49-721-608-47990; E-mail: thomas.seelig@kit.edu

KEYWORDS

Rubber-toughened polymers, multiple crazing, constitutive model, single-edge-notch-tension fracture tests

1 Introduction

The ductility and toughness of various polymeric materials – thermoplastics as well as thermosets – can be substantially improved by mixing-in fine dispersed rubber particles; e.g. [6]. A key effect of the rubber particles is that they enable and initiate inelastic, hence energy absorbing, microscale deformation mechanisms distributed over large regions of the material. The micromechanisms involved in rubber-toughening are *shear yielding* as well as *crazing* in the matrix phase, often preceded by *cavitation* of the rubber particles. The interrelation between these mechanisms and their efficiency (or predominance) in toughening strongly depends on the material at hand. This dependence not only includes the matrix material, the rubber particle size and volume fraction, but also the overall loading conditions (loading rate, temperature and stress triaxiality); e.g. [2],[3],[5],[10],[18],[22],[37]. Moreover, the "type" (e.g. internal structure) of the rubber particles which may vary with the manufacturing process is known to be of some influence, e.g. [6],[16].

Of particular interest in the present work is the role of crazing, i.e. the formation of localized zones in which the bulk polymer is drawn into thin fibrils; e.g. [23]. Crazing in homogeneous polymers clearly is a precursor of brittle failure under tensile loading. In rubber-toughened polymers, however, crazes are trapped in the ligament between the dispersed rubber particles and collectively may give rise to macroscopically large inelastic strains prior to failure, e.g. [21]. The perhaps most prominent example in this regard is high-impact-polystyrene (HIPS) where overall inelastic deformation is exclusively due to distributed crazing. In rubber-toughened thermoplastics with a less brittle matrix such as acrylonitrile-butadiene-styrene (ABS), some "competition" between shear yielding and crazing is observed. In fact, within the large family of ABS materials, experiments have revealed a wealth of different phenomena – from shear yielding induced by cavitating soft rubber particles all the way to distributed crazing around hard 'salami' particles, and almost every combination in between (depending on constitution,

particle size, manufacturing process and loading conditions). Moreover, microstructural studies in [37],[39] confirm that both shear yielding and distributed crazing may occur in the same ABS specimen depending on the distance to the fracture surface. The present work focuses on the role of spatially distributed crazing as shown in Fig. 1.

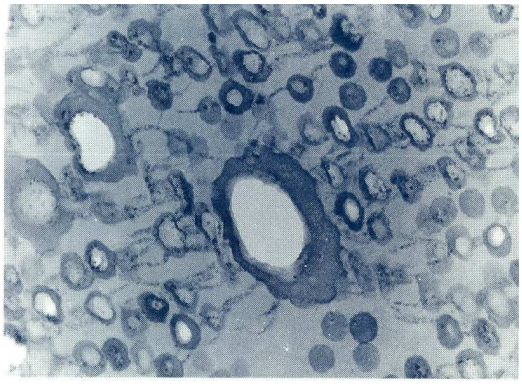

Figure 1: Microstructure of ABS showing extensive crazing between cavitated rubber particles [39]

While a large number of experimental studies have addressed the complex interplay between microstructure, micromechanisms and resulting overall performance (e.g. fracture toughness), appropriate macroscopic material models for rubber-toughened polymers – and in particular those based on the underlying physical mechanisms – are rare, even to date. Before an all-embracing micromechanical description is feasible, theoretical models first have to deliver a deeper understanding of the individual mechanisms (thereby necessarily making simplifying assumptions). The majority of modeling approaches so far has focused on matrix shear yielding in conjunction with void growth from cavitated rubber particles, e.g. [9],[25],[35],[41],[47],[48]. Numerical simulations carried out in [30], however, suggested that such a modeling approach is unable to reproduce the characteristic shape of the plastic zone at a notch in ABS tensile specimens as it tends to overestimate localization of plastic deformation. It was concluded that the effect of distributed crazing cannot be neglected in the overall inelastic deformation behavior of ABS.

Owing to their localized crack-like appearance, individual crazes in neat glassy polymers have successfully been modeled as cohesive surfaces, e.g. in [13],[14] and [43]. Utilizing such a description, the competition between crazing and matrix shear yielding in the vicinity of

a single void, representing a cavitated rubber particle in ABS, was investigated in [33]. The formation of multiple crazes from a rubbery particle in HIPS was modeled numerically using special continuum elements in [34] and [36]. To avoid the necessity of having to trace individual crazes, one may adopt a continuum description of distributed crazing, as proposed for neat glassy polymers (i.e. without particles) in [15]. This model incorporates the kinematics of craze widening by taking the average spacing between crazes as a characteristic length scale.

The objective of the present work is to complement earlier modeling approaches, e.g. [30],[41], which considered inelastic deformation due to shear yielding alone by considering here the opposite extreme, i.e. the effect of *distributed crazing* only. This means that we will ignore shear yielding and make the simplifying key assumptions that, firstly, crazes span the ligament between all the uniformly dispersed rubber particles and, secondly, that (viscoplastic) opening of the crazes is the only source of inelastic deformation. The kinematics of craze opening in the direction of maximum principal tensile stress considered in [15] will be extended to account also for overall shearing as it occurs for instance in the wake of an advancing crack tip. The constitutive model set up in Sect. 2.1 is endowed with scaling relations with respect to microstructural parameters via simple micromechanical considerations in Sect. 2.2. The model is calibrated in Sect. 3 from tensile tests which we performed on a commercial ABS material. In Sect. 4 results of numerical simulations of crack propagation in a notched tensile specimen are presented and analyzed with regard to the influence of the rubber content on the overall fracture toughness. Comparison of model predictions and experimental data will reveal strengths and shortcomings of the present distributed crazing model and provides additional insight into the collective effects of shear yielding and crazing in the overall behavior of ABS.

Throughout the paper, the symbolic bold face notation of vectors $\boldsymbol{a}$ and tensors $\boldsymbol{A}$ is used as well as the index notation a_i , A_{ij} with respect to cartesian base vectors $\boldsymbol{e}_i\,(i = 1, 2, 3)$. Single and double contraction of indices is represented by the symbols " $\cdot$ " and " : ", respectively, and the standard summation convention is employed, e.g., $\boldsymbol{a} \cdot \boldsymbol{b} = a_i b_i$, $\boldsymbol{A} \cdot \boldsymbol{a} = A_{ij} a_j \boldsymbol{e}_i$, $\boldsymbol{A} : \boldsymbol{B} = A_{ij} B_{ij}$. The dyadic product $\otimes$ of two vectors has components $(\boldsymbol{a} \otimes \boldsymbol{b})_{ij} = a_i b_j$.

2 Constitutive modeling

This section is concerned with the formulation of a constitutive model for the overall deformation and failure behavior of rubber-toughened materials such as ABS with focus on the effect of distributed crazing. Overall inelastic deformation in this theory results from the specific kinematics of cohesive crack-like opening of crazes, while the volume fraction and size of rubber particles are explicitly accounted for via micromechanical considerations.

2.1 Homogenized model for distributed crazing

Various experimental studies, e.g. [2],[3],[5],[6],[22],[37], indicate that the inelastic deformation of rubber-toughened polymers such as ABS under tensile loading to a large extent proceeds by the formation of multiple crazes in the ligament between the rubber particles. The crazes initiate from the rubber particles (stress concentrators) and, under continued loading, they collectively grow into mesoscopic band-like damage zones distributed throughout the material, e.g. [2],[22],[28],[31]. Crazes are primarily oriented normal to the direction of maximum principal stress at the instant of their formation. This suggests the picture schematically drawn in Fig. 2 which forms the basis for the model set up in the following.

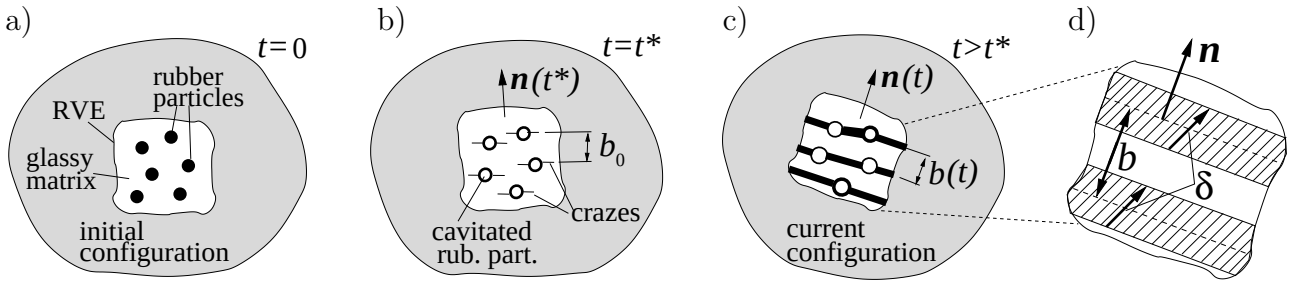

Figure 2: Schematic of successive deformation states of an RVE of the rubber-toughened polymer undergoing distributed craze initiation at time t^* and subsequent craze opening.

A macroscopic material point is taken to correspond to a representative volume element (RVE) of the rubber-toughened polymer (Fig. 2a). As will be motivated in Sect. 2.2 the spherical rubber particles in the present model are assumed to cavitate in the early stage of loading, i.e. prior to the occurrence of crazing; after cavitation they are considered to behave mechanically equivalent to voids. Crazing initiates at time $t = t^*$ when the maximum principal

tensile stress attains a critical value (Fig. 2b); this value will be specified in terms of an effective stress acting on the inter-particle ligament in Sect. 2.2. The craze orientation, defined by the unit normal vector $\boldsymbol{n}$, is determined by the direction of maximum principal stress at initiation. Under continued loading the crazes develop into several localized damage zones which extend over the ligament between the rubber particles (Fig. 2c; see also micrographs in [2] or [28]). The crazed material inside these damage zones consists of numerous thin fibrils spanning the craze-bulk interfaces. Inelastic deformation proceeds by separation of the craze-bulk interfaces (i.e. craze opening) and the damage zones can be considered as cohesive surfaces distributed throughout the RVE. In the current configuration and on the macroscopic level, the kinematics of inelastic deformation is represented by the overall separation vector $\boldsymbol{\delta}$, the craze normal vector $\boldsymbol{n}$ and the average spacing b between the damage zones (Fig. 2d).

In view of the numerical implementation, it is convenient to formulate the constitutive equations in rate form in the current configuration. Therefore, the macroscopic rate-of-deformation tensor $\boldsymbol{D}$ is additively split into an elastic and inelastic part

$$\boldsymbol{D} = \boldsymbol{D}^e + \boldsymbol{D}^c \quad . \tag{1}$$

The inelastic part of the rate-of-deformation tensor represents the effect of distributed crazing in a homogenized sense and, similar to [15], is written as

$$\boldsymbol{D}^c = \frac{1}{b}\left(\dot{\boldsymbol{\delta}} \otimes \boldsymbol{n}\right)^{\mathrm{sym}} = \frac{1}{b}\left(\dot{\delta}_n \boldsymbol{n} \otimes \boldsymbol{n} + \dot{\delta}_\tau (\boldsymbol{\tau} \otimes \boldsymbol{n})^{\mathrm{sym}}\right) \tag{2}$$

where the separation rate vector $\dot{\boldsymbol{\delta}} = \dot{\delta}_n \boldsymbol{n} + \dot{\delta}_\tau \boldsymbol{\tau}$ incorporates components normal and tangential to the crazes with the tangential unit vector $\boldsymbol{\tau}$ specified below. While at the onset of crazing (with the craze orientation $\boldsymbol{n}$ equal to the direction of maximum principal stress) only a normal separation δ_n takes place, the representation (2) also accounts for a possible overall inelastic shearing of the RVE (tangential craze opening δ_τ) associated with non-proportional changes of the stress state in the course of deformation. The unit tangent vector $\boldsymbol{\tau}$ in the corresponding component of $\boldsymbol{D}^c$ in Eq. (2) is defined by the direction of the current resolved shear stress with respect the craze orientation according to

$$\boldsymbol{\tau} = \frac{\boldsymbol{\sigma} \cdot \boldsymbol{n} - \sigma_n \boldsymbol{n}}{\sigma_\tau} \qquad \text{where} \qquad \sigma_n = \boldsymbol{n} \cdot \boldsymbol{\sigma} \cdot \boldsymbol{n} \qquad , \qquad \sigma_\tau = |\boldsymbol{\sigma} \cdot \boldsymbol{n} - \sigma_n \boldsymbol{n}| \tag{3}$$

and $\boldsymbol{\sigma}$ being the Cauchy stress tensor. The average spacing b of the craze zones in (2) is further specified by means of a unit cell model in Sect. 2.2, and a more thorough presentation

of the kinematic micro-to-macro transition in the framework of finite inelastic deformations is provided in the Appendix.

The normal and tangential components $\dot{\delta}_n$ and $\dot{\delta}_\tau$ of the craze opening rate in Eq. (2) result from the microscopic process of drawing of the bulk polymer material into numerous thin fibrils. For a detailed review of the micromechanics of the viscoplastic crazing process based on fundamental experimental investigations the reader is referred to [23]. Following previous work on the continuum mechanical modeling of crazing where individual crazes have been described either as cohesive surfaces, e.g. [13],[33],[43], or using closely related concepts, e.g. [34],[36], the separate Eyring-type relations

$$\dot{\delta}_n = \dot{\delta}_{n0} \exp\left(\frac{A}{T}\left[\tilde{\sigma}_n - \sigma_n^c(\delta_n)\right]\right) \quad , \qquad \dot{\delta}_\tau = \dot{\delta}_{\tau 0} \exp\left(\frac{A}{T}\left[\tilde{\sigma}_\tau - \sigma_\tau^c(\delta_n)\right]\right) \tag{4}$$

are adopted here for the normal and tangential craze opening rates, respectively, where $\dot{\delta}_{n0}$, $\dot{\delta}_{\tau 0}$ and A are material parameters and T is the temperature. In the numerical analyses presented later on in the present work, isothermal conditions are assumed. Yet, the incorporation of adiabatic heating with a changing temperature would easily be feasible through the explicit temperature dependence in (4), e.g. following [14].

The quantities $\tilde{\sigma}_n$ and $\tilde{\sigma}_\tau$ in Eq. (4) are the 'driving stresses' for craze opening in the normal and tangential direction (further discussed in Sect. 2.2) while $\sigma_n^c(\delta_n)$ and $\sigma_\tau^c(\delta_n)$ denote the corresponding resistances ('craze yield strengths') which are both taken to vary with the craze normal opening δ_n. The complete loss of stress carrying capacity due to craze failure is for simplicity assumed here to take place when the total craze opening reaches a critical value δ_{crit}, i.e. at

$$\delta \equiv \sqrt{\delta_n^2 + \delta_\tau^2} = \delta_{\text{crit}} \quad . \tag{5}$$

Alternatively, one might consider a cohesive zone formulation with the traction vector being co-axial to the (total) separation vector as suggested by Van den Bosch et al. [45]. However, while this appears appropriate if the craze matter behaves isotropically or consists of (one-dimensional) 'strings', the choice of two separate relations (4) for the normal and tangential tractions in the present work is motivated by the more complex microstructure of the craze matter containing so-called 'cross-tie' fibrils, e.g. [43].

The function $\sigma_n^c(\delta_n)$ for the resistance against craze widening, i.e. the shape of the traction-separation law in the underlying cohesive surface description of crazing, is a key ingredient of

the present model. A non-monotonic variation featuring softening and rehardening as sketched in Fig. 3 is assumed here, similar to that used in [33]. Such a response appears appropriate

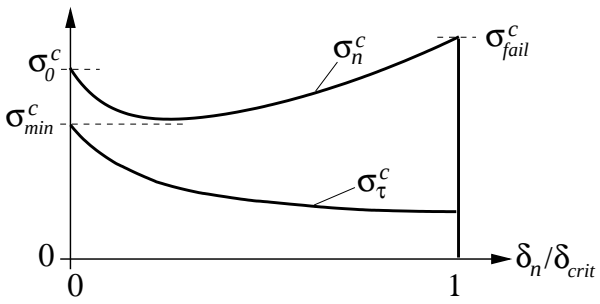

Figure 3: Variation of craze opening resistances with craze width.

for several reasons. Firstly, numerical investigations of the fibril drawing process, either in the framework of continuum mechanics using finite elements, e.g. [1],[20], or by molecular dynamics simulations [32], suggest that the craze stress strongly decreases in the early stage of fibril formation while it increases again when mature fibrils of highly stretched molecules are drawn, up to their ultimate rupture. Secondly, combined experimental/analytical studies, e.g. [11], where the stress variation along a craze was calculated from the measured craze opening profile indicate stress peaks at the craze tip (i.e. at fibril formation) as well as at the end region of a craze, i.e. prior to fibril rupture. As these are qualitative arguments, the quantitative variation $\sigma_n^c(\delta_n)$ is admittedly not firmly established. In the present work the expression

$$\sigma_n^c(\delta_n) = \sigma_{\min}^c + (\sigma_0^c - \sigma_{\min}^c) \exp\left(-h_n \frac{\delta_n}{\delta_{\text{crit}}}\right) + (\sigma_{\text{fail}}^c - \sigma_{\min}^c) \left(\frac{\delta_n}{\delta_{\text{crit}}}\right)^q \tag{6}$$

is assumed and the adjustable parameters σ_0^c, $\sigma_{\min}^c$, σ_{fail}^c, h_n and q are determined by fitting the overall response of the constitutive model to that of a real ABS material (see Sect. 3.1). The particular choice of an exponential decay and power-law hardening in (6) is motivated merely by its suitability in this fitting process. Following [43], the stress-carrying capacity of the craze matter in the tangential direction is assumed to decrease monotonically with the craze opening. This is phenomenologically described here by the function (see also Fig. 3)

$$\sigma_\tau^c(\delta_n) = \sigma_{\min}^c \exp\left(-h_\tau \frac{\delta_n}{\delta_{\text{crit}}}\right) \tag{7}$$

where h_τ is a material parameter.

2.2 Microstructural considerations and scaling relations

As already mentioned in the Introduction, the predominance of shear yielding or crazing in ABS is strongly influenced by the rubber particle type and size (e.g. with smaller ones understood to favor shear yielding, e.g. [10]). Since the emphasis of this study in on the role of crazing alone, we here focus attention on a material with soft rubber particles which cavitate at low stress and afterwards behave mechanically equivalent to voids. This assumption precludes effects like the size dependence of particle cavitation and any load-bearing capacity of the cavitated particles, yet it complies with assumptions made in several earlier studies looking solely at matrix shear yielding to which the present distributed crazing model is to be contrasted. This notion is also supported by detailed numerical studies in [41] where rubber particles with a wide range of cross-link densities have been shown to not contribute significantly to the overall stress after their cavitation.

Key microstructural parameters in the present model hence are the size (radius) r and the volume fraction f of the rubber particles which determine the average initial spacing b_0 between crazes as discussed below. In addition the ultimate craze opening δ_{crit} at craze breakdown plays a pivotal role and introduces a characteristic length which has to be related to the craze spacing. We establish the connection between these quantities by means of simple micromechanical considerations based on the unit cell model sketched in Fig. 4.

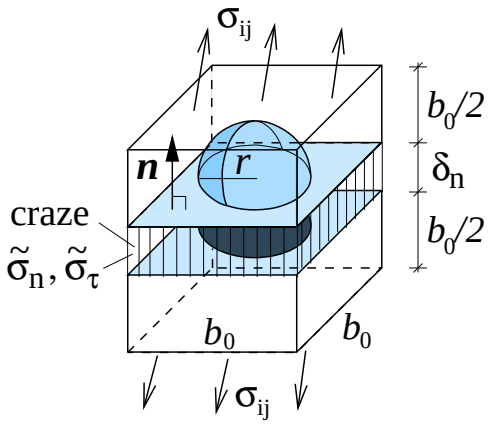

Figure 4: Unit cell of microstructure with single craze in equator region of rubber particle.

Assuming that all the rubber particles have crazes associated with them, we consider a cubic unit cell of size b_0 containing a single rubber particle which is treated as a void after

its cavitation. A craze zone with unit normal $\boldsymbol{n}$ and current width δ_n has formed from the particle's equator region (only normal opening of craze sketched here for simplicity). This setting addresses the situation in materials with homogeneous rubber particles where often only a single craze emanates from a particle. While this is observed in some ABS materials and rubber-toughened PMMA, the large heterogeneous 'salami' particles typically found in HIPS and also some grades of ABS give rise to several crazes initiating from each particle, e.g. [2],[3],[6].

The unit cell size, i.e. the initial spacing b_0 between crazes, is determined by the rubber particle radius r and the volume fraction of rubber particles $f = \frac{4}{3}\pi r^3/b_0^3$. From the latter relation,

$$b_0(r,f) = r\,(4\pi/3f)^{1/3} \approx 1.6\,r f^{-1/3} \quad . \tag{8}$$

Owing to the assumption of a single craze per particle, the current spacing between the centre plane of neighboring crazes introduced in Eq. (2) is given as (see Fig. 4)

$$b = b_0 + \delta_n \quad . \tag{9}$$

Thus, both the rubber particle volume fraction and size are accounted for in the overall inelastic strain rate (2). Furthermore, from the overall resolved normal and shear stress with respect to the craze orientation $\boldsymbol{n}$ and the area fraction $(b_0^2 - \pi r^2)/b_0^2$ of the inter-particle ligament, the effective (i.e. average) normal and shear stresses $\tilde{\sigma}_n$ and $\tilde{\sigma}_\tau$ acting on the craze area are given as

$$\tilde{\sigma}_n = \frac{\boldsymbol{n}\cdot\boldsymbol{\sigma}\cdot\boldsymbol{n}}{1-\pi\,(r/b_0)^2} = \frac{\sigma_n}{1-\pi\,(3f/4\pi)^{2/3}} \approx \frac{\sigma_n}{1-1.2f^{2/3}} \qquad , \qquad \tilde{\sigma}_\tau \approx \frac{\sigma_\tau}{1-1.2f^{2/3}} \quad . \tag{10}$$

The effective stresses $\tilde{\sigma}_n$ and $\tilde{\sigma}_\tau$ enter Eqs. (4) as the driving stresses for viscoplastic craze opening. Moreover, Eq. $(10)_1$ also serves as the criterion for craze initiation with $\tilde{\sigma}_n = \sigma_0^c$ from Eq. (6) and σ_n then being the overall maximum principal tensile stress. This criterion may be augmented with a dependence of σ_0^c on the hydrostatic stress, but in view of the lack of consensus in the literature on this effect we assume here that craze initiation is governed only by principal stress.

Other unit cell types (e.g. body centered cubic) may be considered alternatively; yet, this does not affect the scaling with the rubber content in Eqs. (8) and (10), only the numerical pre-factors of order unity then slightly change. Craze widening, i.e. the conversion from bulk

into fibrillated polymer material, results in a significant overall volume increase. When this takes place in the equator region of a void (cavitated rubber particle) as sketched in Fig. 4, the void itself grows. It can be shown from simple geometrical considerations that the change of the porosity (current ratio of void volume by cell volume) is small in the course of craze widening; this effect is therefore neglected and f is taken constant.

The constitutive model presented above accounts for the microstructure in terms of the physically motivated parameters f, r and $\delta_{\rm crit}$. As further discussed in Sect. 3.2.1, the overall material behavior depends only on the two dimensionless parameters f and $r/\delta_{\rm crit}$.

2.3 Overall elastic behavior including damage

The overall elastic stiffness of rubber-toughened polymers undergoing distributed crazing is affected by the volume fraction of rubber particles, their cavitation, and the amount of crazing. These effects are considered here in a two-step homogenization leading to the 4^{th} order effective elasticity tensor $\mathbf{E}^*$, to be discussed below, governing the macroscopic hypo-elastic relation

$$\overset{\nabla}{\boldsymbol{\sigma}} = \mathbf{E}^* : (\boldsymbol{D} - \boldsymbol{D}^c) \tag{11}$$

where $\overset{\nabla}{\boldsymbol{\sigma}}$ denotes the Jaumann rate of the Cauchy stress tensor.

Neglecting for a moment the presence of craze zones, the microstructure of the material consists of an isotropic linear elastic matrix, with bulk and shear moduli K and μ, and dispersed rubber particles, with bulk and shear moduli K_r and μ_r, respectively. According to the Mori-Tanaka model, see e.g. [17], the overall isotropic effective moduli can be approximated as

$$K^*(f) = \frac{K + [\alpha(1-f)+f](K_r - K)}{1 + \alpha(1-f)(K_r/K - 1)} \quad , \qquad \mu^*(f) = \frac{\mu + [\beta(1-f)+f](\mu_r - \mu)}{1 + \beta(1-f)(\mu_r/\mu - 1)} \tag{12}$$

where f denotes the volume fraction of particles and $\alpha = 3K/(3K+4\mu)$, $\beta = 6(K + 2\mu)/5(3K+4\mu)$. In particular, as the shear modulus of rubber is much smaller than the other elastic constants (Poisson's ratio $\nu_r \approx 0.5$) we set $\mu_r = 0$. The bulk modulus of rubber is not much different from that of a glassy polymer, so we simply take $K_r = K$ prior to cavitation of the particles and set $K_r = 0$ afterwards. This switch in the effective elastic constants due to rubber particle cavitation is for simplicity assumed to take place at a critical value of hydrostatic (mean) stress $\sigma_m^{\rm cav}$. Typical values for the latter are reported to be of the order of

10 MPa; e.g. [25],[31],[41]. More advanced cavitation criteria, e.g. accounting for a particle size dependent cavitation resistance, are discussed e.g. in [19].

In addition, the effective porous medium is considered to experience an evolving damage by distributed crazing. Despite the orientation of crazes, the resulting overall elastic behavior is for simplicity taken to be isotropic since data for the amount of anisotropy due to crazing are currently not available. The effective elastic stiffness $\mathbf{E}^*$ is – besides its dependence on f through Eq. (12) – assumed to decrease monotonically with increasing craze width δ_n according to

$$\mathbf{E}^*\left(f, \delta_n/\delta_{\mathrm{crit}}\right) = \mathbf{E}^*(f)\left(1 + \eta\,\frac{\delta_n}{\delta_{\mathrm{crit}}}\right)^{-1} \quad . \tag{13}$$

Physically, the parameter $\eta \gg 1$ reflects the stiffness ratio of bulk polymer and craze matter, and the relation (13) corresponds to an approximation in which the bulk material and the craze are considered to be in series with respect to the principal loading direction (Fig. 4). However, the parameter η is adjusted to fit experimental data from unloading tests after different amounts of inelastic strain as further discussed in Sect. 3.1.

The material model has been implemented as a user subroutine in the commercial finite element code LS-Dyna [27]. Thereby, an efficient semi-implicit time integration of the constitutive equations is employed where only the scalar quantities δ_n and δ_τ are updated implicitly whereas the tensorial direction of plastic flow is updated in an explicit manner, as suggested e.g. in [4].

3 Model calibration and evaluation

3.1 Material parameter identification from tensile tests

The material model developed in Sect. 2 addresses the situation of a microstructure with a fine dispersion of rubber particles which cavitate at low stress and give rise to the formation of craze zones (typically not more than one per particle) in the surrounding glassy matrix (Fig. 2b,c). This is found in some ABS materials (see Fig. 1) and rubber-toughened PMMA, e.g. [2],[3],[6],[10],[22],[37]. It is important to note that ABS represents a large family of materials with a multitude of different commercial grades which differ in composition, e.g. the amount (typically between 5 and 40 vol.%), size, and morphology (processing-dependent in-

ternal structure) of the rubber particles. In order to analyze in how far the developed model is capable to capture the deformation behavior of *some* real ABS material, tensile tests have been performed on a commercial, off-the-shelf ABS grade without any information about its microstructural constitution.

The material was provided in extruded sheets of 3 mm thickness from which flat testing specimens were machined with the geometry sketched in Fig. 5a. The experiments were carried out on a servo-hydraulic testing machine (Instron) at room temperature and at different constant values of the nominal (engineering) strain rate, i.e. at constant velocity. Uniaxial tensile tests were performed at strain rates of $10^{-4}, 10^{-3}, 10^{-2}, 10^{-1}\,\mathrm{sec}^{-1}$, each with at least three replicates. The specimens were attached to the machine by mechanical clamps. In the course of deformation the in-plane strain field in the center region of the flat specimens (Fig. 5a) was analyzed using 2D digital image correlation (DIC, Limess Co. [26]) with a camera resolution of 2 MPixel and a maximum frame rate of $20\,\mathrm{sec}^{-1}$. As visible from Fig. 5b at two levels of

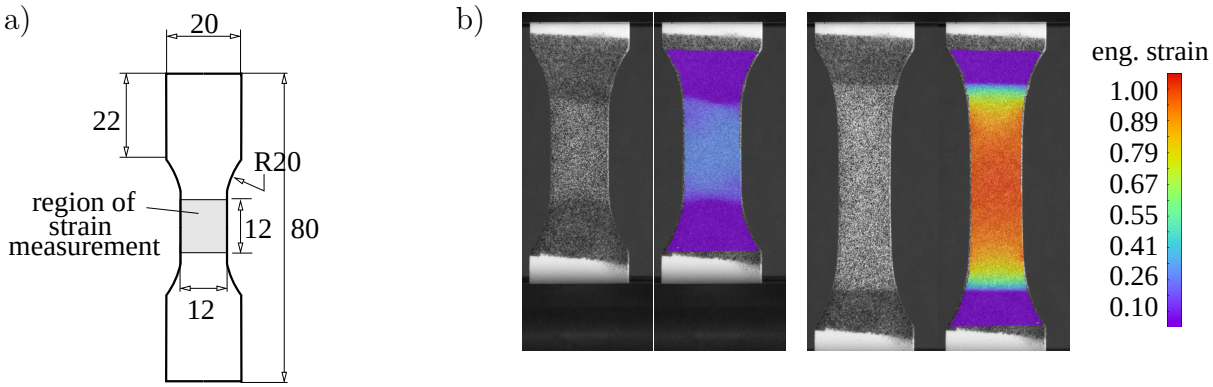

Figure 5: a) Sketch of tensile specimen used (values in mm, thickness 3 mm), b) contours of strain in tensile direction at two different deformation stages obtained from DIC.

deformation, the strain in the specimen center region remained fairly homogeneous throughout the tests, i.e. necking did not take place. Since only the strains in the specimen plane were measured, the determination of the current specimen cross section was based on the assumption that the strain in thickness direction equals the in-plane transverse strain. Hence, the true (Cauchy) stress σ is computed from the force F, the engineering transverse strain ε_{tr} and the

initial (undeformed) cross section A_0 according to

$$\sigma = \frac{F}{A_0(1+\varepsilon_{tr})^2} \quad . \tag{14}$$

True stress vs. engineering strain curves obtained in this manner are shown in Fig. 6a for a few identical tests along with the response of the adjusted material model. The experimental data show a rather small amount of scatter, even in the strain at failure. The tested material displays an almost linear elastic behavior with Young's modulus $E^* \approx 1500\,\mathrm{MPa}$ and Poisson's ratio $\nu^* \approx 0.42$ up to a distinct yield point at about 2% strain and a stress of $\sigma \approx 32\,\mathrm{MPa}$. This yield point is followed by a stress drop until $\sigma \approx 27\,\mathrm{MPa}$ and subsequent rehardening until abrupt failure, typically occurring when σ has passed 40 MPa and at an engineering strain between 1.15 and 1.25. The measured initial Young's modulus E^* and Poisson's ratio ν^* in conjunction with corresponding literature data for the SAN matrix properties, e.g. [41], were used here to determine the rubber content from the analytical relations (12); a rough estimate of $f \approx 0.2$ was thus obtained. Afterwards the yield strength relation $\sigma_n^c(\delta_n/\delta_{\mathrm{crit}})$ according to (6) was fitted so that the overall response of the model with $f = 0.2$ agrees with the experimental stress-strain curve (Fig. 6a). The engineering strain in the tensile direction is related to the craze width δ_n through $\varepsilon = \sigma/E^* + \delta_n/b_0$ in view of the small elastic strains $\sigma/E^* \ll 1$. According to Eqs. (2),(8) and (9) the critical craze width at failure δ_{crit} is related to the spacing between crazes which scales with the rubber particle radius. From fitting the model response to the experimentally observed failure strain, we obtain a value of $r/\delta_{\mathrm{crit}} = 0.6$. This means that craze failure takes place at a craze width of about 80% of the rubber particle diameter, which is consistent with other experimental observations, e.g. [2],[28]. The effect of variations in the microstructural parameters f and r/δ_{crit} on the model response will be further discussed in Sect. 3.2.1.

The strain rate dependence of the tested ABS material in comparison with the model response is shown in Fig. 6b (for clarity and in view of the small amount of scatter only one experimental curve per strain rate is shown). The experiments show that the yield strength increases by approximately 5 MPa per decade of strain rate. After adjusting the material parameters A and $\dot{\delta}_{n0}/\delta_{\mathrm{crit}}$ in $(4)_1$ a reasonable agreement is obtained over four decades of strain rate. In view of the lack of corresponding experimental data, the rate parameter $\dot{\delta}_{\tau 0}$ of tangential craze opening in (4) is set equal to that in normal direction, i.e. $\dot{\delta}_{\tau 0} = \dot{\delta}_{n0}$.

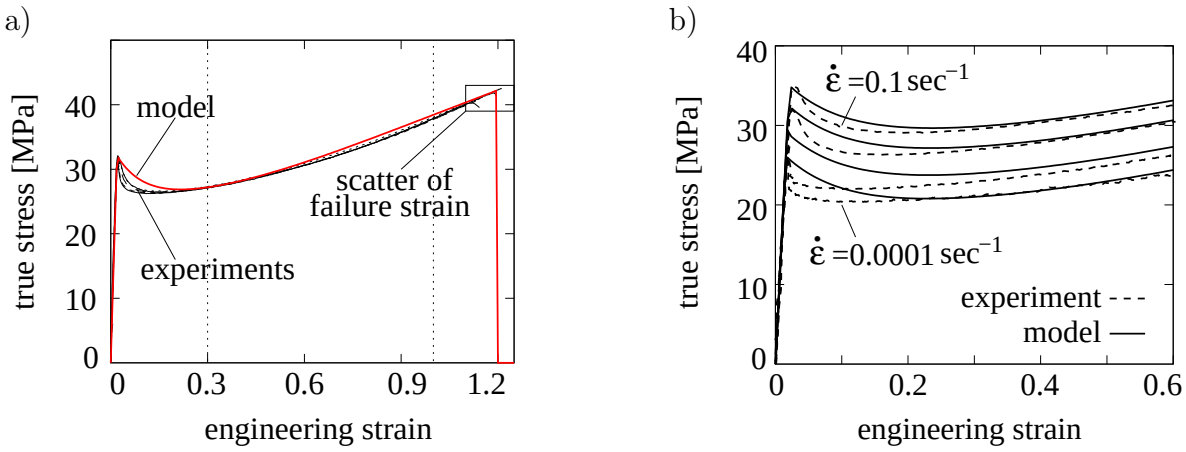

Figure 6: a) Uniaxial true stress vs. engineering strain response of commercial ABS and calibrated model (at $\dot{\varepsilon} = 10^{-2}\text{sec}^{-1}$), b) strain rate dependence under uniaxial tension in the range $\dot{\varepsilon} = 10^{-4}...10^{-1}\text{sec}^{-1}$.

Uniaxial cyclic tensile tests (dashed line in Fig. 7a) show hysteresis and a decreasing unloading-reloading slope with increasing inelastic deformation. This indicates that damage evolution takes place. The slope of the secant through the unloading-reloading hystereses at different values of inelastic deformation represents the reduction of the elastic stiffness. A decreasing overall stiffness in the material model was fitted to the experimental data by adjusting the parameter η in Eq. (13). The model response under repeated unloading and reloading is depicted by the solid curve in Fig. 7a. Not captured by the model is the hysteresis in the experimental data which is likely to be caused by viscoelastic effects. These effects are not accounted for in the present viscoplastic approximation of the craze behaviour. The full set of the material parameters thus determined are summarized in Tab. 1.

The widening of distributed crazes on the micro-scale results in a significant amount of dilation in the macroscopic inelastic strain. This can already be conjectured from the small amount of specimen contraction seen in Fig. 5b. As mentioned before, the experimental determination of the volumetric strain from the 2D strain field in the specimen plane is based on the assumption that the strain in the thickness direction is equal to the in-plane transverse strain. The evolution of volumetric strain with axial strain obtained from experiments at three different strain rates is shown in Fig. 7b along with the model response which is optically indistinguishable for the three strain rates. The model captures the general trend well, but

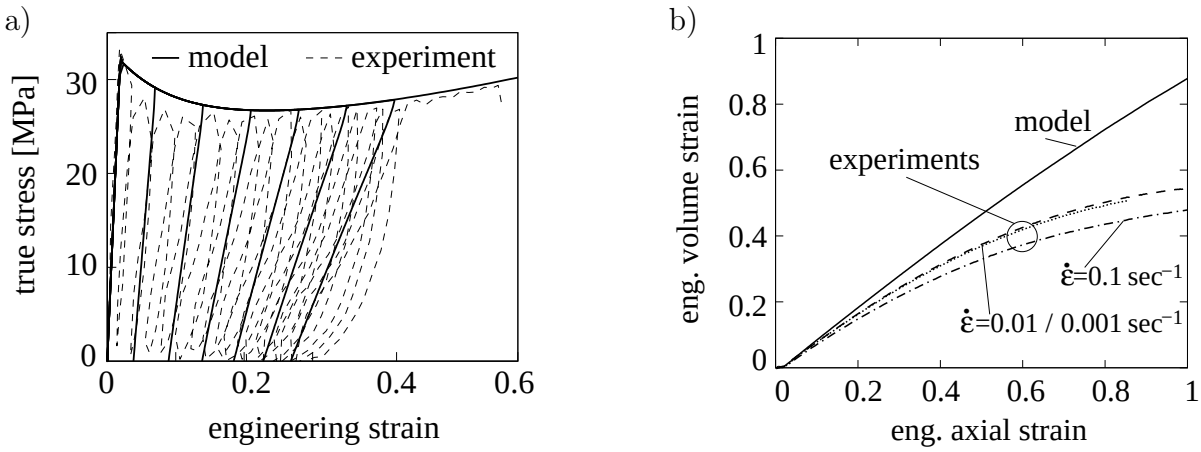

Figure 7: Comparison of experimental results with model response under uniaxial tension showing: a) effect of unloading after different levels of straining (at $\dot{\varepsilon} = 10^{-2}\text{sec}^{-1}$), and b) evolution of volumetric vs. axial strain at different strain rates.

it overestimates the volume strain under macroscopic uniaxial loading. Consistent with the assumption that inelasticity is exclusively due to crazing, the model yields a volume strain which is approximately equal to the axial strain. The deviation of the model response from the present experimental data for ABS suggests that in this material some amount of matrix shear yielding takes place, as observed also e.g. in [47]. By contrast, micromechanical and homogenized models of rubber-toughened polymers accounting only for matrix shear yielding, e.g. [9],[41], when subjected to macroscopic uniaxial tension, predict overall volume strains of only a few percent of the axial strain and hence deviate much more from the experimental data in Fig. 7b. This emphasizes the role of distributed crazing in ABS even at low stress triaxialities.

E [MPa]	ν [-]	A [K/MPa]	$\dot{\delta}_{n0}/\delta_{\text{crit}}$ [sec^{-1}]	$\dot{\delta}_{\tau 0}/\delta_{\text{crit}}$ [sec^{-1}]	σ_0^c [MPa]	σ_{min}^c [MPa]	σ_{fail}^c [MPa]	h_n [-]	h_τ [-]	q [-]	r/δ_{crit} [-]	η [-]	f [-]
2550	0.38	150	10^{-4}	10^{-4}	40	30	55	33	1	2	0.6	15	0.2

Table 1: Material parameters determined by adjusting the model to experimental data

3.2 Influence of microstructural parameters

3.2.1 Effect of rubber content and rubber particle size

Various experimental studies have indicated that the volume fraction f as well as the size r of the rubber particles have a strong influence on the overall deformation behavior of ABS materials, e.g. [5],[18],[21],[40],[42],[46]. The ultimate craze width δ_{crit} at craze failure (cf. Eq. (5)) is in the present work assumed to be constant and provides a length scale to which the rubber particle size can be related. The effect of the two dimensionless microstructural parameters f and r/δ_{crit} is explicitly accounted for in the presented material model via the flow rule (2) and the micromechanical scaling relations (8)-(10). Figure 8 shows the variation of the model response with these parameters under uniaxial tension in comparison to the experimental data to which the model has been calibrated ($f = 0.2$, $r/\delta_{\text{crit}} = 0.6$). The decrease in stress level and the increase in ductility (failure strain) with increasing rubber content f shown in Fig. 8a result from the scaling relations (8) and (10) utilized in the model (see also the discussion in Sect. 3.2.2) and qualitatively correspond well to what is reported from experimental studies, e.g. [21],[44]. Yet, quantitatively the effect of f on the failure strain of ABS appears to be underestimated by the model in comparison with experimental findings in [21] where the failure strain progressively increased with increasing rubber content. This discrepancy might be due to the effects of matrix shear yielding as well as craze bridging by highly stretched rubber particles, which both are not accounted for in the present model.

As shown in Fig. 8b, the model predicts larger failure strains for smaller values of the rubber particle size r (at fixed δ_{crit}). This can be explained from the proportionality between the particle size r and the craze spacing b_0 (at fixed volume fraction f) according to Eq. (8) from which a larger contribution of craze widening to the overall RVE strain results for smaller rubber particles. Experimental studies, e.g. [18],[40],[46], have revealed a rather complex and manifold influence of the rubber particle size on the overall mechanical behavior of ABS, and results in [46] indeed display an increasing failure strain for smaller particles in a range of strain rates comparable to that in Fig. 8. However, the model prediction according to Fig. 8b has to be taken with caution since rubber particle size effects reported from experimental studies are likely to be attributed to a switch in the microscopic deformation mechanisms, i.e. the suppression of crazing in favor of matrix shear yielding for smaller particles, e.g. [10], which is not considered in the present model.

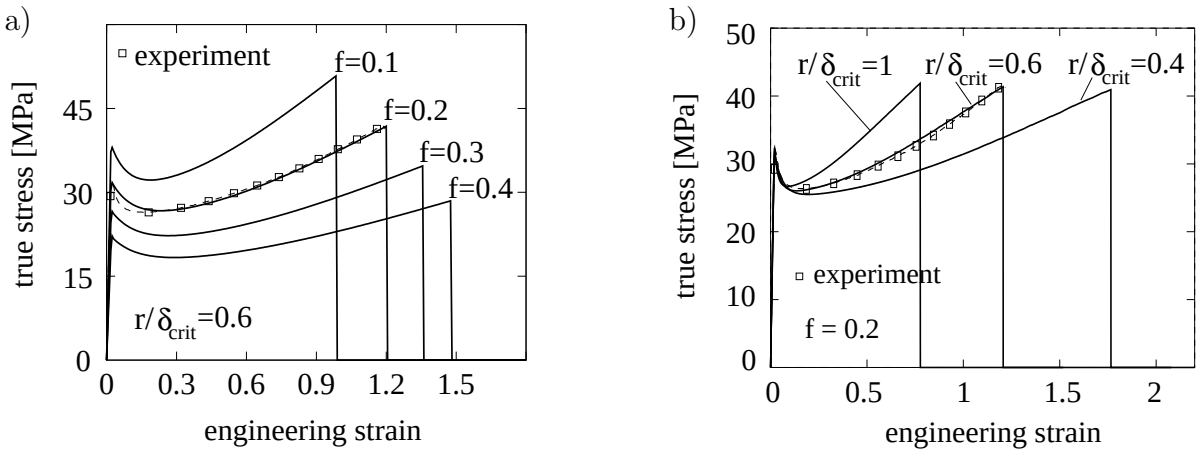

Figure 8: a) Effect of rubber content f (porosity) and b) effect of ratio r/δ_{crit} on model response under uniaxial tension at strain rate $\dot{\varepsilon} = 0.01\text{sec}^{-1}$.

3.2.2 The issue of an optimal rubber content

The main reason for modifying polymer materials with a rubbery phase is to enhance their ductility and fracture toughness. Hence, the quest for an optimal rubber content is of key practical importance. This issue will be briefly discussed here in the framework of the suggested material model for distributed crazing under uniaxial loading; it will be further analyzed in Sect. 4.2 through finite element simulations of the more realistic situation of 3D fracture tests.

From the unit cell considerations in Sect. 2.2 the logarithmic macroscopic inelastic strain at failure, i.e. at $\delta_n = \delta_{\text{crit}}$, is given by

$$\varepsilon_{\text{fail}}(f) = \ln\left(\frac{b_0 + \delta_{\text{crit}}}{b_0}\right) \approx \ln\left(1 + \frac{\delta_{\text{crit}}}{r}\, f^{1/3}\right) \quad . \tag{15}$$

The overall stress normal to the craze zones, on the other hand, scales with the rubber content f according to (10) as

$$\sigma_n(f) \approx \sigma^c \left(1 - f^{2/3}\right) \tag{16}$$

where σ^c denotes the craze yield strength. If the latter is taken constant for the present considerations, the product $w_{\text{fail}} = \sigma_n\, \varepsilon_{\text{fail}}$ represents the specific (i.e. per volume) work until failure of the material and can be taken as a measure of toughness. Figure 9 shows w_{fail} computed from the analytic expressions (15),(16) and normalized by the (constant) craze yield strength σ^c as a function of the rubber content (solid curve). Also shown (symbols • in Fig. 9)

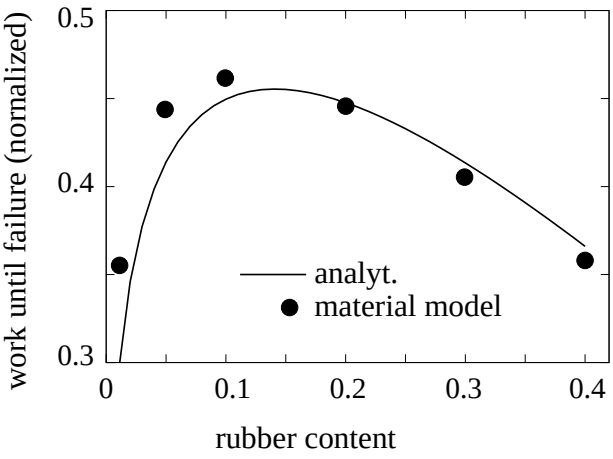

Figure 9: Specific work until failure vs. rubber content f according to the estimate (15),(16) with constant craze stress and the exact model response according to Fig. 8a.

is the exact constitutive model response $w_{\text{fail}}^{\text{ex}} = \int_0^{\varepsilon_{\text{fail}}} \sigma_n \, \mathrm{d}\varepsilon$ under uniaxial tension at a strain rate of $\dot{\varepsilon} = 0.01\text{sec}^{-1}$ and normalized by σ_{fail}^{c} (see Tab. 1). From both evaluations it can be seen that the specific work until failure displays a non-monotonic dependence on the rubber content with a maximum at some intermediate value of $f \approx 0.1...0.15$.

This finding might be taken as a theoretical indication for the existence of an optimum rubber content with respect to the toughness of rubber-toughened polymers undergoing predominantly distributed crazing. However, the discussion so far considers homogeneous deformations whereas experimental studies indicating an optimal toughness depending on the rubber content comprise fracture tests, e.g. [5],[42]. Corresponding results from numerical simulations of fracture experiments are presented in Sect. 4.2.

4 Fracture behavior of SENT specimen

In order to assess in how far the developed constitutive model is capable of describing the fracture behavior of ABS materials, a single-edge-notch-tension (SENT) specimen, see Fig. 10, is considered in the following. Though not appropriate for the determination of "true" fracture properties (e.g. crack resistance curves) such a specimen type is occasionally utilized in polymer testing, e.g. [37],[40]. Some measure of the material's fracture toughness, referred to as the

specific work of fracture, is then obtained in terms of the total work exerted on the specimen until complete fracture divided by the fracture surface area. Thus, no distinction is made between the actual work of separation and the work dissipated in the plastic zone surrounding the fracture surface. The advantage of this type of test, however, lies in the fact that it is very easy to perform. Moreover, it allows to analyze the characteristic plastic zone that develops ahead of the notch prior to fracture (Sect. 4.1.1) both experimentally, using DIC, and numerically, using the homogenized material model. The use of the latter is justified since the length scale associated with the strain gradient resulting from the blunt notch is sufficiently large compared to the microstructural length scale (rubber particle size or spacing). Findings from the present work then may be directly compared with detailed results presented by Steenbrink et al. [37] who used the same specimen type.

While the primary aim of this work is the development and analysis of the constitutive model (Sect. 2) as well as its application in numerical simulations, we have also performed fracture experiments on the commercial ABS material used before for the model calibration. The experimental data then serve to analyse the performance of the model as discussed in Sect. 4.1. The SENT specimen geometry is depicted in Fig. 10a, and the 3D finite element mesh used in the numerical simulations is shown in Fig. 10b. Since the specimen of 80 mm

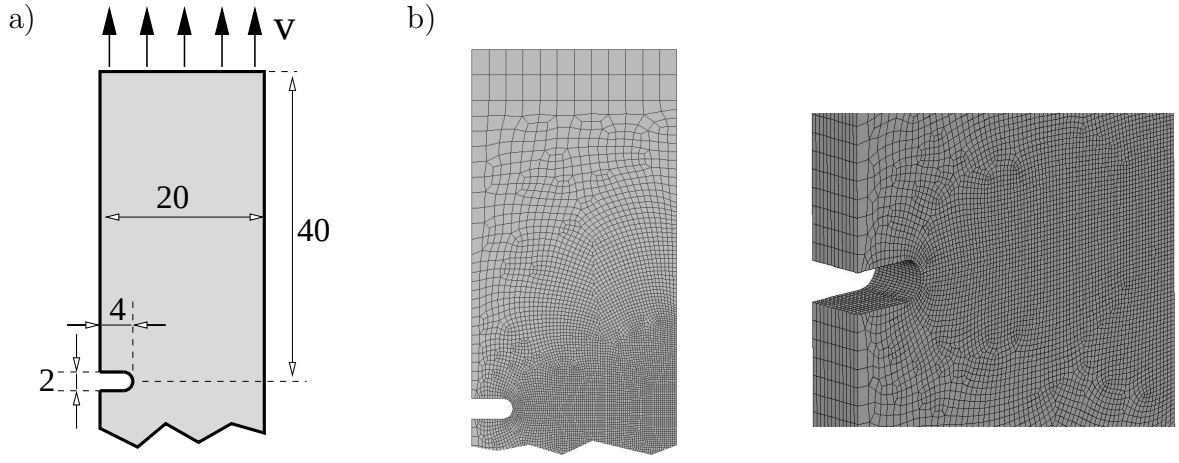

Figure 10: a) Sketch of SENT specimen (values in mm, thickness 3mm), b) parts of finite element mesh.

length was clamped at the ends in the testing device the specimen length free to deform in the computational model was reduced to 70 mm. The velocity of specimen extension (relative

clamp motion) was $v = 1\,\mathrm{mm/sec}$ in the experiments as well as in the simulations. Also, all tests and simulations were performed at room temperature. In a similar way as during the uniaxial tension tests, see Sect. 3.1, the tests were monitored by a digital camera, facilitating a post-test determination of the in-plane strain fields by DIC.

4.1 Experimental vs. computational results

4.1.1 Plastic zone formation at notch

The enhanced fracture toughness of rubber-toughened polymers corresponds to the formation of a large plastic zone (sometimes referred to as "stress-whitened" owing to its optical appearance) that develops at a crack tip or notch under tensile loading. A characteristic feature of the plastic zone in rubber-toughened thermoplastics such as ABS, e.g. [29],[31], but observed also in rubber-toughened epoxies, e.g. [12], is its *elongated shape* which is understood to result from the specific inelastic micro-mechanisms (rubber particle cavitation, void growth in conjunction with matrix shear yielding, crazing). It fundamentally differs from the bulky plastic zones typically observed in metals or homogeneous ductile glassy polymers under plane strain conditions, e.g. [24], which can well be reproduced in numerical simulations using established material models. Attempts to reproduce the elongated plastic zone in rubber-toughened polymers by computational models, however, so far have not been very successful. In particular, in a previous study [30] where void growth in a matrix undergoing plastically incompressible shear yielding was considered the dominant (sole) damage mechanism in ABS, the resulting softening in the homogenized material response led to an unrealistic narrow plastic zone. In contrast, Tijssens et al. [43] employed multiple spatially distributed cohesive zones to describe distributed crazing in a neat glassy polymer and obtained an inelastic deformation zone at a circular hole in a plate which was in reasonable agreement with experimental observations. In order to complement the above mentioned studies, we here apply the model presented in Sect. 2 and 3, which focuses on the effect of distributed crazing and deliberately ignores shear yielding, to the situation of a notched tensile (SENT) specimen.

Experimental and numerical results for the inelastic deformation zone in front of the notch are shown in Fig. 11 for two successive loading stages, i.e. overall specimen elongations of 1.4 mm (I) and 2.4 mm (II), respectively. The contour plots depict the strain at the specimen surface in the tensile (vertical) direction – which is almost equal to the maximum principal

strain – obtained from digital image correlation and the finite element simulation, respectively. Obviously, the characteristic elongated shape of the plastic zone is well captured by the simu-

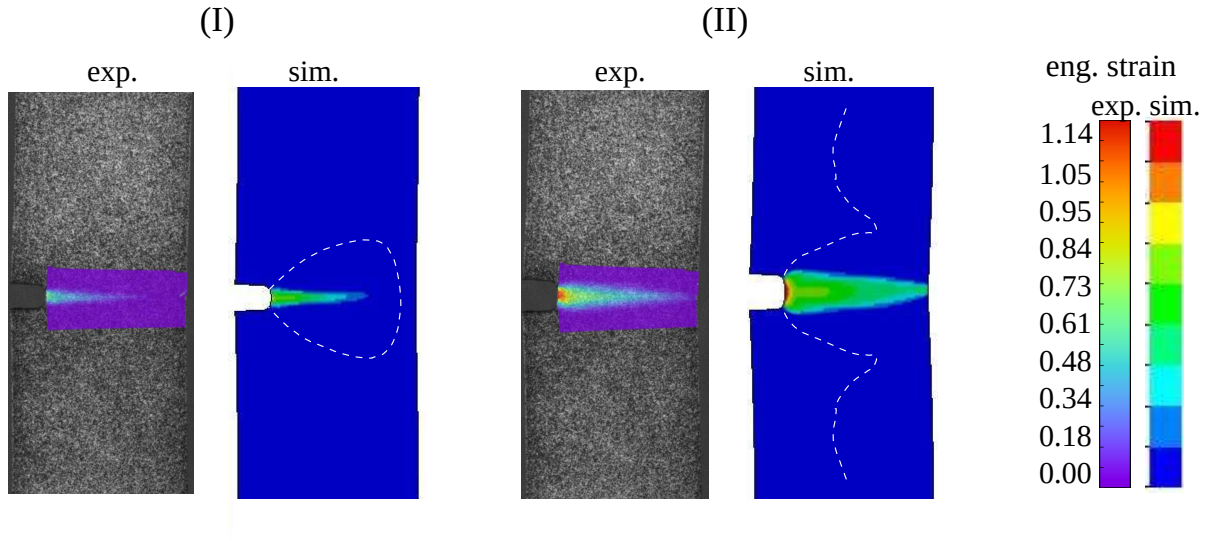

Figure 11: Experimentally and numerically determined distribution of strain in vertical direction in SENT specimen at loading stages (I) and (II) indicated in Fig. 12a. Dashed contours indicate region inside which rubber particle cavitation at an assumed critical hydrostatic stress $\sigma_m^{cav} = 10\,\mathrm{MPa}$ has occurred in the simulation.

lations. Owing to the model ingredients, the spreading of inelastic deformation in a narrow zone ahead of the notch is favored by the overall dilation in the material model (due to craze widening) in conjunction with the initial softening (Figs. 6 and 7b). The lateral extension of this zone over the entire width of the notch, on the other hand, is attributed to the subsequent rehardening. The hardening remains present in the response of the distributed crazing model also under notch tip loading conditions with a higher stress-triaxiality than in Fig. 6a. In contrast, a porous plasticity model accounting solely for matrix shear yielding, even when endowed with progressive matrix hardening, in such a situation inevitably displays overall softening [38] which results in a far too localized plastic zone in finite element simulations [30].

Also shown by the dashed lines in Fig. 11 is the region inside which rubber particle cavitation at an assumed critical hydrostatic stress of $\sigma_m^{cav} = 10\,\mathrm{MPa}$ has occurred in the simulation. The bulky shape of the cavitation zone which engulfs the elongated plastic zone in Fig. 11 in the early stage of loading (I) corresponds quite well to what is reported from experiments, e.g. [29],[39],

and also analytical considerations based on contours of hydrostatic stress, e.g. [7].

4.1.2 Crack propagation

Crack advance is realized in the simulations by removing finite elements from the model when the critical craze opening is reached, i.e. at $\delta = \delta_{\text{crit}}$ according to (5). Figure 12a shows the overall response of the SENT specimen in terms of force vs. displacement curves from three experimental tests and the numerical simulation. The stages indicated by (I) and (II)

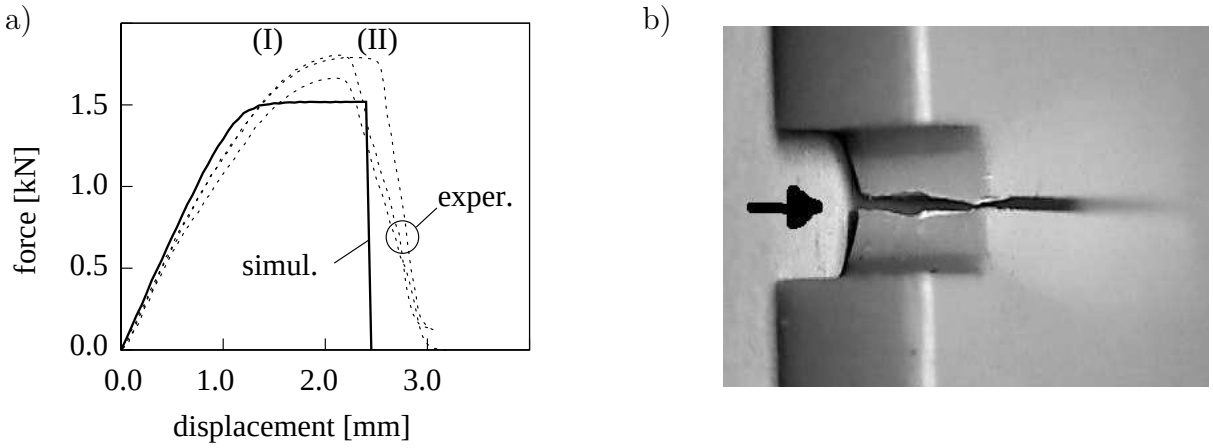

Figure 12: a) Force vs. displacements curves for SENT specimen from experiments and simulation, b) fractured specimen indicating some amount of necking.

at a relative displacement of the specimen ends of about 1.4 mm and 2.4 mm, respectively, correspond to the snapshots of the plastic zone in Fig. 11. Stage (I) refers to the beginning of the plateau region in the force-displacement curve in Fig. 12a, and it is seen from Fig. 11 that at this stage the plastic zone has not yet extended over the entire ligament length. Stage (II) indicates the situation right before specimen failure. Though the simulation reasonably captures the general trend of the experimental force-displacement curves, and in particular the deformation at fracture, several deviations are to be noticed. In comparison with the experimental data, the simulated force-displacement curve displays a somewhat stiffer response during the initial rise and a more abrupt change towards the load plateau. Maximum load values are higher in the experiments which also appear to display a more stable crack propagation during the final load drop (yet, measurements in this regime may be not very reliable). These deviations are

likely to be attributed to the lack of any inelastic deformation mechanism other than crazing in the present material model in which the effect of matrix shear yielding has deliberately been ignored. In fact, the close-up view of a fractured test specimen in Fig. 12b shows a larger degree of plastic deformation at the specimen surface, i.e. at lower stress triaxiality, along with some amount of necking, both being indicative of matrix shear yielding. In the numerical simulations where crazing is considered to be the only inelastic deformation mechanism and stress triaxiality is of minor importance, such a inhomogeneous deformation over the specimen thickness was not observed.

4.2 Effect of rubber content on fracture toughness

In Fig. 13a force vs. displacement curves from simulated SENT tests are shown for different values of the rubber content f. With increasing f the overall force decreases while the displacement until failure increases. The corresponding specific work of fracture (i.e. area under force-displacement curve divided by ligament area of 16 mm×3 mm) is shown in Fig. 13b as a function of the rubber content. The simulations predict a maximum work of fracture for a

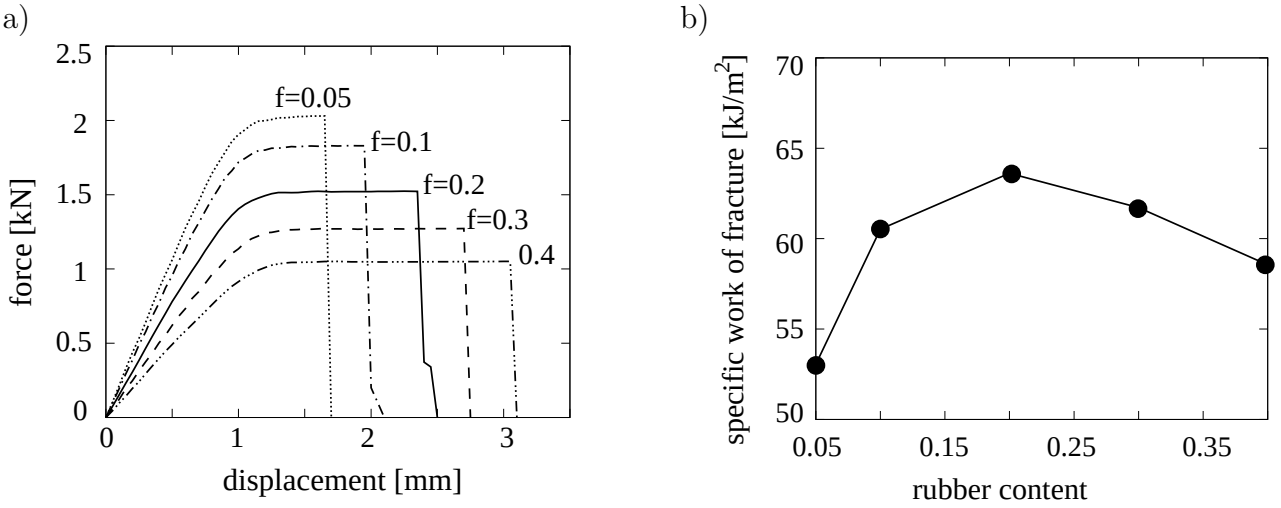

Figure 13: Effect of rubber content on simulated SENT fracture tests: a) force vs. displacement curves, b) dependence of specific work of fracture on rubber content.

rubber content of $f \approx 0.2$, which is rather similar to what was observed in case of uniaxial tension (Fig. 9) as well as from experiments in [5] and [42]. The absolute values of the specific

work of fracture in Fig. 13b, in turn, are close to the experimental results in [37] obtained using the same type of test specimen as considered in our simulations. In their series of fracture experiments (with more detailed results in [39]), however, the fracture energy showed a slight monotonic increase with increasing rubber content instead of an intermediate maximum.

5 Discussion and conclusions

Toughening in ABS materials is mediated by two dissipative micromechanisms, i.e. shear yielding and crazing. In order to analyse the sole effect of spatially distributed crazing a homogenized material model was developed in the framework of large inelastic strains that deliberately ignores shear yielding and assumes crazing to be the only source of inelasticity. In this way the model complements earlier studies, e.g. [9],[30],[35],[41],[47], where the opposite extreme was considered, namely the effect of shear yielding alone. In contrast to porous plasticity models accounting only for matrix shear yielding, e.g. [30], the present *distributed crazing model* proves to be more successful in reproducing the characteristic elongated shape of the plastic zone in front of a (mode I loaded) notch. This is due to the ability of the distibuted crazing model to accommodate overall dilation without reducing the load-carrying capacity of the ligament between voids as it inevitably happens by void growth in a plastically incompressible (shear yielding) matrix.

Experimental tests have been conducted on a commercial ABS material of unknown composition (e.g. rubber content) under uniaxial as well as notched tensile conditions. The constitutive model has been calibrated to capture the stress-strain response of the real ABS material under uniaxial monotonic and cyclic tensile loading at different strain rates. It turned out that, by accounting solely for crazing, the material model overestimates volumetric strain under uniaxial tension; this indicates that in the real ABS some amount of matrix shear yielding takes place. However, models that consider only matrix shear yielding, significantly underestimate the evolution of volume strain at low stress triaxialities. The comparison of these complementing modeling approaches hence provides important information for the future development of more realistic models comprising both mechanisms. While the present model has been calibrated to experimental data in uniaxial tension, it is also applied in simulations with more complex stress states and reasonably captures the fracture behavior of the tested ABS material in case of the

considered SENT specimen. Again, deviations from experimental data can, at least partly, be ascribed to the absence of shear yielding which has been ignored in our model.

Variations of microstructural parameters yield a model response that is qualitatively consistent with experimental findings in the literature. In particular, the model predicts a maximum of the fracture toughness at some intermediate value of the rubber content of about 20%, similar to experimental observations in [5],[42]. The model also predicts some influence of the rubber particle size with smaller particles leading to a larger strain at failure. The correspondence of this effect with experimental findings, however, has to be taken with caution since the influence of rubber particle size on the inelastic deformation behavior of rubber-toughened polymers, and in particular ABS, appears to be far more complex than captured by the present model, see e.g. [18],[19]. For instance, the question whether crazing or matrix shear yielding is the dominant deformation mechanism in ABS is strongly connected to the rubber particle size, with very small particles being less efficient for initiating crazes. Moreover, the particle size may affect several other factors of influence on the overall material behavior such as the particle cavitation resistance or particle clustering, e.g. [40]. In fact, the microstructure considered in our model is strongly idealized as we assumed all rubber particles to have the same size and to all cavitate simultaneously, whereas in real ABS often a more complex (e.g. bimodal) size distribution prevails, e.g. [19], and only a certain percentage of the particles undergo cavitation and act as craze initiators, e.g. [2],[22],[28]. Also, rubber particles in real materials may be not as well dispersed as assumed in the model. Interesting insight into the effects of rubber particle size and volume fraction in rubber toughening may be gained from analytical considerations using linear elastic fracture mechanics, e.g. [7],[8]; yet, these concepts are not easily extended to the situation of large inelastic strains addressed by the present computational model as well as those mentioned in the Introduction.

Since the model presented here pertains to materials with homogeneous soft rubber particles which do not carry much load after cavitation (as motivated in Sect. 2.2), the overall hardening response (see, e.g., Fig. 6) is entirely ascribed to the behavior of the crazed matrix material in the inter-particle ligament via Eq. (6). It should, however, be noted that in materials like HIPS (and those ABS grades with a similar microstructure) the rubbery phase in the heterogeneous 'salami'-type particles also undergoes fibrillation and has been conjectured to contribute to the overall stress at large stretches, e.g. [19],[34].

The shortcomings of the model revealed by the present study suggest amendments in several regards. Firstly, a more realistic description of ABS materials should account for both of the mentioned microscopic deformation mechanisms, i.e. crazing *and* matrix shear yielding. The transition between them then might be controlled primarily by the stress triaxiality and the strain rate, with lower values of both parameters promoting shear yielding. Strain rate, in turn, appears to be a parameter that affects the crazing process itself via the competing mechanisms of disentanglement and chain scission [23] with some influence e.g. on the craze width at failure, hence δ_{crit} in our model. Also, temperature effects – completely excluded in the present work – should be accounted for since they are naturally connected with strain rate in polymer deformation, and experimental studies on rubber-toughening are often performed under impact conditions where adiabatic heating may take place. Finally, the overall anisotropy that develops in the course of deformation due to the orientation of the craze zones has been neglected so far. Recent experimental studies on pre-stretched ABS (to be reported elsewhere) in fact indicate a significant amount of anisotropic damage that probably should be considered in a more refined model for the deformation history dependent behavior of rubber-toughened polymers.

Acknowledgements

Financial support of this work by the German Science Foundation (DFG) under grant no. SE 872/5 is gratefully acknowledged. We would also like to thank the German Academic Exchange Service (DAAD) for financial support of a stay of M.H. at SIMLab/Trondheim where part of the experiments were performed. The authors gratefully acknowledge also the assistance of the laboratory staff at SIMLab and KIT.

Appendix

The transition from the microscopic inelastic deformation mechanisms of crack-like cohesive surface opening sketched in Fig. 2 towards the kinematics of macroscopic elastic-inelastic deformation according to Eqs. (1) and (2) is elaborated here in more detail. Therefore, a representative volume element (RVE; see Fig. 2) of the microstructure in the undeformed reference configuration is taken as a domain of volume V_0 and exterior boundary ∂V_0 which contains

surfaces of discontinuity with respect to the displacement and hence the current position $\boldsymbol{x}$ of material points $\boldsymbol{X}$ (position vector in ref. config.), collectively denoted as Γ_0. The local defor-

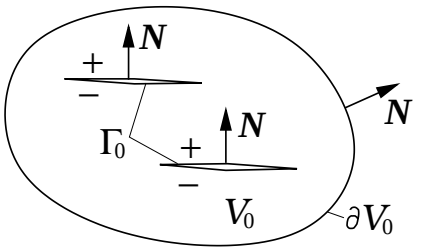

Figure 14: Schematic of continuum with crack-like discontinuity surfaces considered in micro-to-macro transition (17).

mation gradient tensor $\boldsymbol{F}_{cont} = \dfrac{\partial \boldsymbol{x}}{\partial \boldsymbol{X}}$ is assumed to be continuous throughout the matrix phase $V_0 \backslash \Gamma_0$ of the RVE, while solely on Γ_0 a discontinuity in terms of a local separation vector (jump) $[\![\boldsymbol{x}]\!] := \boldsymbol{x}|_{\Gamma_0^+} - \boldsymbol{x}|_{\Gamma_0^-}$ prevails. With the positive and negative sides ('crack-flanks') Γ_0^+ and Γ_0^- of the discontinuity surface (Fig. 14) the total boundary of the matrix phase is $\partial V_0 \cup \Gamma_0^+ \cup \Gamma_0^-$, and $\boldsymbol{N}$ denotes the unit normal vector of any external or internal boundary in the reference configuration. Taking the volume average of $\boldsymbol{F}_{cont}$ over the matrix phase and applying the divergence theorem to the latter leads to the definition of the macroscopic deformation gradient of the RVE as

$$\bar{\boldsymbol{F}} := \frac{1}{V_0} \int\limits_{\partial V_0} \boldsymbol{x} \otimes \boldsymbol{N} \, \mathrm{d}A_0 = \frac{1}{V_0} \int\limits_{V_0 \backslash \Gamma_0} \boldsymbol{F}_{cont} \, \mathrm{d}V_0 + \frac{1}{V_0} \int\limits_{\Gamma_0} [\![\boldsymbol{x}]\!] \otimes \boldsymbol{N} \, \mathrm{d}A_0 \quad . \tag{17}$$

It consists of the volume average of the continuous local deformation gradient plus a contribution due to material separation on the discontinuity surfaces Γ_0.

Motivated by experimental observations on rubber-toughened polymers, e.g. in [2],[28], we now assume that the unit normal vector on the discontinuity surfaces (i.e. crazes) is constant throughout the RVE. This allows to define the average separation vector $\boldsymbol{\delta}$ on the RVE through

$$\boldsymbol{\delta} := \frac{1}{|\Gamma_0|} \int\limits_{\Gamma_0} [\![\boldsymbol{x}]\!] \, \mathrm{d}A_0 \tag{18}$$

where $|\Gamma_0|$ denotes the total area of the discontinuity surfaces inside V_0. If we furthermore introduce the average spacing between discontinuity surfaces in the reference configuration of

the RVE as $b_0 := \dfrac{V_0}{|\Gamma_0|}$ the representation of the macroscopic deformation gradient simplifies to

$$\bar{\boldsymbol{F}} = \frac{1}{V_0} \int\limits_{V_0 \setminus \Gamma_0} \boldsymbol{F}_{cont} \, \mathrm{d}V_0 + \frac{1}{b_0} \, \boldsymbol{\delta} \otimes \boldsymbol{N} \quad . \tag{19}$$

In accordance with the discussion of the model for distributed crazing in Sect. 2.1 we assume that separation on the discontinuity surfaces (crazes) is the only source of inelasticity in the RVE and elastic deformations are locally described by $\boldsymbol{F}_{cont}$. As a consequence, we define the elastic part of the macroscopic deformation gradient as

$$\bar{\boldsymbol{F}}^{\,e} := \frac{1}{V_0} \int\limits_{V_0 \setminus \Gamma_0} \boldsymbol{F}_{cont} \, \mathrm{d}V_0 \quad . \tag{20}$$

Adopting the common multiplicative split $\bar{\boldsymbol{F}} = \bar{\boldsymbol{F}}^{\,e} \cdot \bar{\boldsymbol{F}}^{\,c}$ of the (macroscopic) deformation gradient into this elastic part and an inelastic part $\bar{\boldsymbol{F}}^{\,c}$ due to crazing, the latter is obtained from (19) and (20) as

$$\bar{\boldsymbol{F}}^{\,c} = \boldsymbol{I} + \frac{1}{b_0} \, \boldsymbol{\Delta} \otimes \boldsymbol{N} \tag{21}$$

where $\boldsymbol{\Delta} := \bar{\boldsymbol{F}}^{\,e-1} \cdot \boldsymbol{\delta}$ denotes the pull-back of the (macroscopic) separation vector $\boldsymbol{\delta}$ to the inelastic intermediate configuration and $\boldsymbol{I}$ is the second-order unit tensor. The Sherman-Morrison formula then yields

$$\bar{\boldsymbol{F}}^{\,c-1} = \boldsymbol{I} - \frac{\boldsymbol{\Delta} \otimes \boldsymbol{N}}{b_0 + \Delta_n} \qquad \text{where} \quad \Delta_n = \boldsymbol{\Delta} \cdot \boldsymbol{N} \tag{22}$$

so that with the material time derivative of (21)

$$\dot{\bar{\boldsymbol{F}}}^{\,c} = \frac{1}{b_0} \, \dot{\boldsymbol{\Delta}} \otimes \boldsymbol{N} \tag{23}$$

we get the inelastic part of the macroscopic velocity gradient the intermediate configuration as

$$\dot{\bar{\boldsymbol{F}}}^{\,c} \cdot \bar{\boldsymbol{F}}^{\,c-1} = \frac{\dot{\boldsymbol{\Delta}} \otimes \boldsymbol{N}}{b_0 + \Delta_n} \quad . \tag{24}$$

The macroscopic velocity gradient in the current configuration and its elastic and inelastic parts follow from

$$\bar{\boldsymbol{L}} = \dot{\bar{\boldsymbol{F}}} \cdot \bar{\boldsymbol{F}}^{-1} = \left(\dot{\bar{\boldsymbol{F}}}^{\,e} \cdot \bar{\boldsymbol{F}}^{\,c} + \bar{\boldsymbol{F}}^{\,e} \cdot \dot{\bar{\boldsymbol{F}}}^{\,c} \right) \cdot \bar{\boldsymbol{F}}^{\,c-1} \cdot \bar{\boldsymbol{F}}^{\,e-1} = \underbrace{\dot{\bar{\boldsymbol{F}}}^{\,e} \cdot \bar{\boldsymbol{F}}^{\,e-1}}_{\bar{\boldsymbol{L}}^{e}} + \underbrace{\frac{\bar{\boldsymbol{F}}^{\,e} \cdot \dot{\boldsymbol{\Delta}} \otimes \boldsymbol{N} \cdot \bar{\boldsymbol{F}}^{\,e-1}}{b_0 + \Delta_n}}_{\bar{\boldsymbol{L}}^{c}} \quad . \tag{25}$$

Assuming now that the elastic strains are small (see e.g. [4] and note the similarity with the kinematics of single crystal plasticity except for the normal opening Δ_n) we may write

$$\bar{\boldsymbol{F}}^{\,e} \cdot \dot{\boldsymbol{\Delta}} \approx \dot{\boldsymbol{\delta}} \qquad \text{and} \quad \boldsymbol{N} \cdot \bar{\boldsymbol{F}}^{\,e-1} \approx \boldsymbol{n} \qquad \text{and} \quad \Delta_n = \boldsymbol{\Delta} \cdot \boldsymbol{N} \approx \boldsymbol{\delta} \cdot \boldsymbol{n} = \delta_n \tag{26}$$

with the separation rate vector $\dot{\boldsymbol{\delta}}$ and the unit vector $\boldsymbol{n}$ in the current configuration so that

$$\bar{\boldsymbol{L}} = \bar{\boldsymbol{L}}^{\,e} + \bar{\boldsymbol{L}}^{\,c} \qquad \text{where} \quad \bar{\boldsymbol{L}}^{\,c} \approx \frac{\dot{\boldsymbol{\delta}} \otimes \boldsymbol{n}}{b_0 + \delta_n} \quad . \tag{27}$$

Taking the symmetric part of (27) and omitting the overbar (introduced in this Appendix merely to indicate macroscopic quantities) we recover (1) in conjunction with (2) and (9).

References

[1] Basu, S., Mahajan, D.K., Van der Giessen, E., 2005. Micromechanics of the growth of a craze fibril in glassy polymers. Polymer 46, 7504-7518.

[2] Beahan, P., Thomas, A., Bevis, M., 1976. Some observations on the micromorphology of deformed ABS and HIPS rubber-modified materials. J. Mat. Sci. 11, 1207-1214.

[3] Beguelin, P., Plummer, C.J.G., Kausch, H.H., 1999. Deformation mechanisms in toughened PMMA. In: Shonaike, G.O., et al. (eds.), Polymer Blends and Alloys, Marcel Dekker Inc., 549-573.

[4] Belytschko, T., Liu, W.K., Moran, B., Elkhodary, K.I., 2013. Nonlinear Finite Elements for Continua and Structures. Wiley

[5] Bernal, C.R., Frontini, P.M., Sforza, M., Bibbo, M.A., 1995. Microstructure, deformation and fracture behavior of commercial ABS resins. J. App. Pol. Sci. 58, 1-10.

[6] Bucknall, C.B., 1977. Toughened Plastics. Applied Science, London.

[7] Bucknall, C.B., Paul, D.R., 2009. Notched impact behavior of polymer blends: Part 1. New model for particle size dependence. Polymer 50, 5539-5548.

[8] Bucknall, C.B., Paul, D.R., 2013. Notched impact behavior of polymer blends: Part 2. Dependence of critical particle size on rubber particle volume fraction. Polymer 54, 320-329.

[9] Danielsson, M., Parks, D.M., Boyce, M.C., 2007. Micromechanics, macromechanics and constitutive modeling of the elasto-viscoplastic deformation of rubber-toughened glassy polymers. J. Mech. Phys. Solids 55, 533-561.

[10] Donald, A.M., Kramer, E.J., 1982. Plastic deformation mechanisms in poly(acrylonitrile-butadiene styrene) ABS. J. Mat. Sci. 17, 1765-1772.

[11] Donald, A.M., Kramer, E.J., Bubeck, R.A., 1982. The entanglement network and craze micromechanics in glassy polymers. J. Pol. Sci. 20, 1129-1141

[12] Du, J., Thouless, M.D., Yee, A.F., 1998. Development of a process zone in rubber-modified epoxy polymers. Int. J. Frac. 92, 271-285.

[13] Estevez, R., Van der Giessen, E., 2005. Modeling and Computational Analysis of Fracture of Glassy Polymers. Adv. Pol. Sci. 188, 195-234.

[14] Estevez, R., Basu, S., Van der Giessen, E., 2005. Analysis of temperature effects near mode I cracks in glassy polymers. Int. J. Frac. 132, 249-273.

[15] Gearing, B.P., Anand, L., 2004. On modeling the deformation and fracture response of glassy polymers due to shear-yielding and crazing. Int. J. Solids Structures 41, 3125-3150.

[16] Giaconi, G.F., Castellani, L., Maestrini, C., Ricco, T., 1998. Development of toughness in ABS resins. Polymer 39, 6315-6324.

[17] Gross, D., Seelig, Th., 2011. Fracture mechanics – with an introduction into micromechanics. Springer.

[18] Han, Y., Lach, R., Grellmann, W., 2001. Effects of rubber content and temperature on unstable fracture behavior in ABS materials with different particle sizes. J. Appl. Pol. Sci. 79, 9-20.

[19] Haward, R.N., Young, R.J. (Eds.), 1997. The Physics of Glassy Polymers. Chapman & Hall.

[20] Helbig, M., Seelig, Th., 2012. Micro-mechanical modeling of fibrillation in amorphous polymers. Comp. Mat. Sci. 52, 118-122.

[21] Ishikawa, M., 1995. Stability of plastic deformation and toughness of polycarbonate blended with poly(acrylonitrile-butadiene-styrene) copolymer. Polymer 36, 2203-2210.

[22] Jar, P.-Y.B., Creagh, D.C., Konishi, K., Shinmura, T., 2002. Mechanical properties and deformation mechanisms in high thermal resistant poly(acrylonitrile-butadiene-styrene) under static tension and izod impact. J. Appl. Pol. Sci. 85, 17-24.

[23] Kramer, E.J., Berger, L.L., 1991. Fundamental processes of craze growth and fracture. In: Crazing in Polymers Vol. 2 (Ed. H.H. Kausch), 1-68, Springer.

[24] Lai, J., Van der Giessen, E., 1997. A numerical study of crack-tip plasticity in glassy polymers. Mech. Mater. 25, 183-197.

[25] Lazzeri, A., Bucknall, C.B., 1993. Dilatational bands in rubber-toughened polymers. J. Mat. Sci. 28, 6799-6808.

[26] Limess, 2009. Digital Image Correlation. Q-400 Operation Manual. Krefeld.

[27] LSTC, 2007. Livermore Software Technology Corporation (LSTC). LS-DYNA keyword user's manual, version 971.

[28] Michler, G.H., 1998. Microstructural construction of polymers with improved mechanical properties. Polym. Adv. Technol. 9, 812-822.

[29] Ni, B.Y., Li, J.C.M., Berry, V.K., 1991. Plastic zone in front of a mode I crack in acrylonitrile-butadiene-styrene polymers. Polymer 32, 2766-2770.

[30] Pijnenburg, K.G.W., Seelig, Th., Van der Giessen, E., 2005. Successively refined models for crack tip plasticity in polymer blends. Eur. J. Mech. A/Solids 24, 740-756.

[31] Ramaswamy, S., Lesser, A.J., 2002. Microscopic damage and macroscopic yield in acrylonitrile-butadiene styrene (ABS) resins tested under multi-axial stress states. Polymer 43, 3743-3752.

[32] Rottler, J., Robbins, M.O., 2003. Growth, microstructure, and failure of crazes in glassy polymers. Phys. Rev. 68, 011801-20131-201318.

[33] Seelig, Th., Van der Giessen, E., 2009. A cell model study of crazing and matrix plasticity in rubber-toughened glassy polymers. Comp. Mat. Sci. 45, 725-728.

[34] Sharma, R., Socrate, S., 2009. Micromechanics of uniaxial tensile deformation and failure in high impact polystyrene (HIPS). Polymer 50, 3386-3395.

[35] Smit, R.J.M., Brekelmans, W.A.M., Meijer, H.E.H., 2000. Predictive modelling of the properties and toughness of polymeric materials; part II: effect of microstructural properties on the macroscopic response of rubber-modified polymers. J. Mat. Sci. 35, 2869-2879.

[36] Socrate, S., Boyce, M.C., Lazzeri, A., 2001. A micromechanical model for multiple crazing in high impact polystyrene. Mech. Mater. 33, 155-175.

[37] Steenbrink, A.C., Janik, H., Gaymans, R.J., 1997. Deformation and fracture of styrene-acrylonitril copolymer-rubber blends. J. Mat. Sci. 32, 5505-5511.

[38] Steenbrink, A.C., Van der Giessen, E., 1997. Void growth in glassy polymers: effect of yield properties on hydrostatic expansion. Int. J. Damage Mech. 6, 317-330.

[39] Steenbrink, A.C., 1998. On deformation and fracture of amorphous polymer-rubber blends. PhD thesis, TU Delft, The Netherlands.

[40] Steenbrink, A.C., Litvinov, V.M., Gaymans, R.J., 1998. Toughening of SAN with acrylic core-shell rubber particles: particle size effect or cross-link density?. Polymer 39, 4817-4825.

[41] Steenbrink, A.C., Van der Giessen, E., 1999. On cavitation, post-cavitation and yield in amorphous polymer-rubber blends. J. Mech. Phys. Solids 47, 843-876

[42] Tan, Z.Y., Xu, X.F., Sun, S.L., Zhou, C., Ao, Y.H., Zhang, H.X., 2006. Influence of rubber content in ABS in wide range on the mechanical properties and morphology of PC/ABS blends with different composition. Polym. Eng. Sci. 46, 1476-1484.

[43] Tijssens, M.G.A., Van der Giessen, E., Sluys, L.J., 2000. Modeling of crazing using a cohesive surface methodolgy. Mech. Mater. 32, 19-35.

[44] Truss, R.W., Chadwick, G.A., 1976. Tensile deformation behavior of ABS polymers. J. Mat. Sci. 11, 111-117.

[45] Van den Bosch, M.J., Schreurs, P.J.G., Geers, M.G.D., 2007. A cohesive zone model with a large displacement formulation accounting for interfacial fibrilation. Eur. J. Mech. A/Solids 26, 1-19.

[46] Xu, X.Y., Xu, X.F., 2011. Mechanical properties and deformation behaviors of Acrylonitrile-Butadiene-Styrene under Izod impact test und unixaial tension at various strain rates. Pol. Eng. Sc. 51, 902-907

[47] Zaïri, F., Nait-Abdelaziz, M., Gloaguen, J.M., Lefebvre, J.M., 2008. Modelling of the elasto-viscoplastic damage behavior of glassy polymers. Int. J. Plast. 24, 945-965.

[48] Zaïri, F., Nait-Abdelaziz, M., Gloaguen, J.M., Lefebvre, J.M., 2011. A physically-based constitutive model for anisotropic damage in rubber-toughened glassy polymers during finite deformation. Int. J. Plast. 27, 25-51

List of Figures

Figure 12: a) Force vs. displacements curves for SENT specimen from experiments and simulation, b) fractured specimen indicating some amount of necking.

Figure 13: Effect of rubber content on simulated SENT fracture tests: a) force vs. displacement curves, b) dependence of specific work of fracture on rubber content.

Figure 14: Schematic of continuum with crack-like discontinuity surfaces considered in micro-to-macro transition (17).

List of Tables